



Hydrogenation of NO_x into ammonia under ambient conditions: From mechanistic investigation to multiphase catalysis

Junxia Yang¹, Lei Sun¹, Tie Yu^{*}, Xu Fang, Shengliang Zhai, Ling Zhang, Guoqing Ren, Rui Tu, Dong Zhai, Zhen Li, Weiqiao Deng^{*}

Institute of Molecular Sciences and Engineering, Institute of Frontier and Interdisciplinary Science, Shandong University, Qingdao, Shandong 266237, China

ARTICLE INFO

Keywords:

Ammonia production
NO_x elimination
Hydrogenation reaction
Covalent triazine framework
Palladium catalysts

ABSTRACT

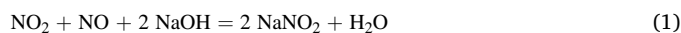
This work proposes a NO_x recycling approach through nitrite hydrogenation into ammonia (NH₃/NH₄OH), and the screened out Pd⁰/Pd²⁺-loaded heterogeneous catalyst achieves excellent ammonia yield. Initially, the DFT calculation of nitrite hydrogenation was conducted to study the determining step for N₂/ammonia generation and guide the catalyst design. Consequently, the designed Pd^{2+/0}/Covalent Triazine Framework (CTF) presented 100% nitrite conversion with 100% ammonia selectivity. The XPS and H₂-TPR results demonstrated the Pd²⁺/Pd⁰ ratios and Pd²⁺ reducibility greatly affected the nitrite conversion and ammonia selectivity. DRIFTS examined the reaction intermediates and the impact of Pd distribution behind ammonia generation. Under ambient conditions, a model test from NO_x adsorption to ammonia release has been completed, and it exhibited an overall conversion of 70% NO_x into ammonia in a single cycle with TOF of 3.9 h⁻¹, which proposes a direction of NO_x recycling and utilization with less energy consumption and free of CO₂ emissions.

1. Introduction

Nowadays, recycling exhaust gases (CO₂, CH_x, NO_x and et al.) as resources to synthesize valuable chemicals could reduce the direct air pollution from exhaust gases emission and relieve supplying pressure for specific chemicals. NO_x pollutants in the atmosphere mainly come from stable source (power plant and et al.) and mobile source (vehicles and et al.), and their annual emissions are above 10 million tons worldwide, which causes acid mist, acid rain, and ozone destruction and harms the human respiration system [1–3]. There have been many NO_x elimination technologies according to NO_x emission source, such as selective catalytic reduction by ammonia (NH₃-SCR) or NO_x storage and reduction (NSR), which convert NO_x into N₂ and release directly [4,5]. Considering the nitrogen cycle in an ecosystem (Schematic 1a), directly turning NO_x into nitrates, nitrites, ammonium ion or other nitrogenous products as resources greatly save energy consumption for nitrogen fixation and across N₂ (N≡N bond energy: 941 kJ/mol) hydrogenation into ammonia [6]. For instance, if NO_x from stable sources such as power stations could be utilized as the nitrogen source and transformed into ammonia through electro-catalysis method for fertilizer production, this will distinctly restrains NO_x emissions and provide alternative

approach for ammonia production simultaneously.

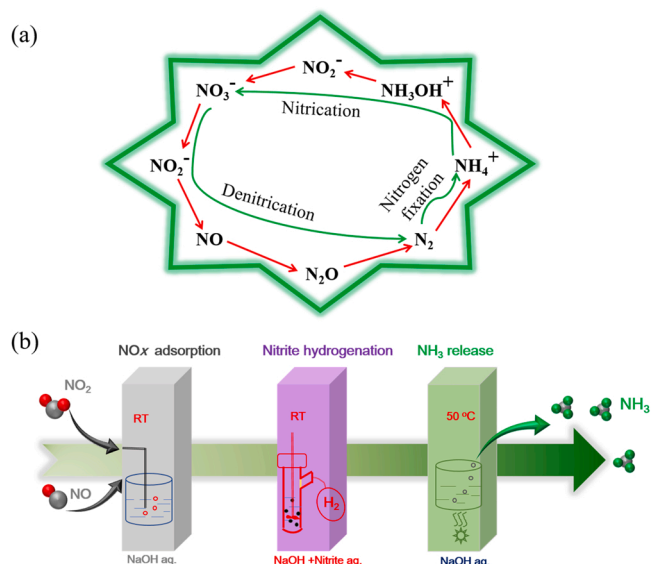
Long and et al. proposed NO reduction route into ammonia through electro-catalysis method, which was more active than N₂ reduction route. Cu foam electrode was screened out to be the optimal active catalyst for NO reduction, and the ammonia generation rate achieved a state-of-the-art 517.1 μmol·cm⁻¹·h⁻¹. The highest Faradaic efficiency was 93.5% at −0.9 V potential, while the N₂ and N₂O started to appear with time on stream. The calculation results demonstrated the superior ammonia selectivity was induced by favorable potentials for ammonia generation over copper electrode [7]. Besides, other experimental or theoretical calculation literatures also dedicated to explore stable catalysts and enhance catalytic performance and ammonia yield through reaction conditions optimization [8–10]. Nevertheless, the inferior NO_x solubility in aqueous system limits the ammonia total yield and the pH value of solution normally affects the reduction products distribution and reaction equilibrium. It is well known that NO_x adsorption in basic solution could turn into nitrites according to Eq. (1), which presents excellent solubility and gives a good indication to boost ammonia total yield.



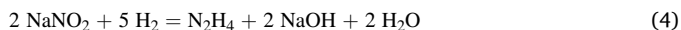
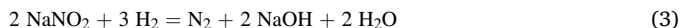
^{*} Corresponding authors.

E-mail addresses: yutie@sdu.edu.cn (T. Yu), dengwq@sdu.edu.cn (W. Deng).

¹ Junxia Yang and Lei Sun contribute equally to this work.



Schematic 1. (a) Simplified scheme of the “classical” nitrogen cycle. (b) NO_x recycling as resource through selective hydrogenation of nitrite into ammonia under ambient conditions.



The nitrites/nitrates hydrogenation has been widely studied through thermo-catalysis, electro-catalysis and photo-catalysis methods so far [11,12]. In the beginning, nitrates hydrogenation is applied to eliminate the nitrogenous pollutants in the sewage treatment, and the N₂ is the desired products for its nontoxicity and ammonia is considered as undesired by-product. Pintar and et al. used Pd/Cu bimetallic catalyst to eliminate nitrates from water, and it was documented the nitrites was the intermediates for nitrates hydrogenation. The presence of nitrites would not affect the N₂ selectivity, while the increment of pH value could inhibit nitrates reaction rates [13,14]. Subsequently, nitrites/nitrates hydrogenation is utilized to synthesize ammonia, especially by electro-catalysis method. Ren and et al. prepared Cu@Cu₂O nanowires and used it for electroreduction of nitrates to ammonia, and the ammonia yield rate achieved 576.53 μg·h⁻¹·mg_{cat}⁻¹ and ammonia Faradaic efficiency was 87.07% at potential -1.2 V vs. saturated calomel electrode [15]. Besides, Wei et al. report that both nitrate and nitrite can be hydrogenated to ammonia by dinickel phosphide with up to 96% selectivity [16]. The related studies about nitrates/nitrites reduction to ammonia mainly focus on efficient catalysts exploration through screening the active metals and supports, controlling the metal distribution and so on, while the nitrates/nitrites conversion and ammonia selectivity still needed to be further improved [17–20].

Combining the above nitrites/nitrates literatures progress, it is seen that the reactants concentrations are low and the solution pH value affects the N₂ or ammonia selectivity. In order to improve the potential for ammonia production in aqueous system, we design an alternative approach in Schematic 1b to achieve a record ammonia yield through nitrite hydrogenation utilizing NO_x as resources. Primarily, transform gaseous NO_x is transformed into nitrite through NO_x adsorption in alkaline solution, and then the nitrite in absorbent solution is hydrogenated to ammonia directly over a heterogeneous catalyst under ambient conditions. The advantages for this approach are no pollutants emission directly since the alkaline solution could be cycled after NO_x adsorption and nitrites hydrogenation, and the whole process is conducted under ambient conditions without additional heating operation.

Since the NO_x transformation into nitrite is easily achieved through adsorption in alkaline solution, the key point of research in this approach concentrates on precisely regulating the product selectivity of nitrite hydrogenation and designing efficient nitrite hydrogenation catalyst under versatile conditions. As shown in reactions (2)–(4), we initially investigated the hydrogenation mechanism to inhibit the side reaction pathway, which provided clues for the catalyst design. Some previous studies have reported that noble metal catalysts could hydrogenate nitrate or nitrite into ammonia or N₂ [21–23], as noble metal catalysts such as palladium (Pd) could provide active hydrogen (H) species through facile hydrogen dissociation [24]. Nevertheless, to design a desired catalyst and selectively reduce nitrite into ammonia still remain a grand challenge. Enlightened by synergy cooperation between single atom sites and nanoparticle species [25–27], we combined theoretical and experimental studies to design a Pd single atom/nanoparticle co-existence catalyst with CTF as the support [28–31] for its rich porous structure and excessive N structure to anchor metal species. The desired catalytic synergy between Pd²⁺ and Pd⁰ in this catalyst improved the nitrite conversion to 100% and the ammonia selectivity to ~100% without other detected byproducts. C₃N₄ [32] and SiO₂ [33] which possess porous structures and different functional groups, were chosen as supports for control experiments to estimate the influence of Pd distribution and coordination on the catalytic activity and selectivity.

2. Experimental

2.1. Preparation of catalysts

The preparation of CTF employed an ionothermal synthesis method described in previous reports [34–36]. First, 2, 6-dicyanopyridine and zinc chloride (ZnCl₂) were ground in a glovebox according to a weight ratio of 3 g/15.9 g, and then the mixture was sealed in a quartz tube with a spacious antrum under vacuum conditions. The sealed mixture was then calcined in a muffle furnace at 400 °C for 20 h and 600 °C for 20 h with a ramping rate of 2 °C/min, since 600 °C was conducive to improving the surface area of CTF. Afterward, the generated black solid was washed 5 times by hot water to remove the residual ZnCl₂, followed by intense stirring in hydrochloric acid solution (2 M) and filtration. Finally, the obtained sample was washed by deionized water/tetrahydrofuran (THF) several times and dried in a vacuum oven overnight at 100 °C. In addition to CTF, C₃N₄ and SiO₂ were chosen as references to elucidate the palladium-support interaction on metal dispersion and activity. The C₃N₄ support was prepared based on a previously reported procedure [37], which was synthesized by a functional NaHCO₃ template-mediated synthesis strategy. The SiO₂ support was purchased from Beijing Mreda Technology INC and used directly without other treatment.

Herein, the Pd species were introduced to supports through impregnation method and Pd^{2+/0}/CTF was exemplified to explain the procedure. First, 500 mg CTF and 82.5 mg of Pd(TFA)₂ were added into 20 mL deionized water and stirred for 12 h at RT under N₂ protection. Then, the suspension was filtered and washed by deionized water several times. The solid product was finally dried in a vacuum oven and pretreated with H₂ at 350 °C for 15 min prior to the reaction.

2.2. Characterization

X-ray diffraction (XRD) was recorded on an Empyrean-100 X-ray diffractometer with a Cu Kα radiation source (λ = 1.541 Å) at 40 mA and 40 kV in the range of 10°–90°. N₂ isotherms were obtained at 77 K on a Quantachrome autosorb iQ2 gas adsorption analyzer. Prior to the test, all samples were degassed at 250 °C for 8 h. The Pd loading was determined by inductively coupled plasma atomic emission spectrometry (ICP-OES, Varian Vista Axial Instrument), while the N and C contents were examined through an organic element analyzer (Elementar vario EL cube, Germany). Transmission electron microscopy (TEM,

TECNAI G2 F20 200 keV, USA) was used to investigate the morphology and noble metal dispersion. Atomic resolution high-angle annular dark-field scanning transmission electron microscopy (HAADF-STEM) images were obtained on an FEI Titan STEM/TEM microscope equipped with a probe corrector. Before imaging, the powder was dissolved in anhydrous ethanol and lightly dusted onto 230 mesh Cu grids coated with ultrathin carbon membrane.

H₂-TPR and CO pulse were conducted on a Micromeritics AutoChem II 2920 with TCD as the detector. Prior to the H₂-TPR measurement, 0.1 g sample was pretreated with Ar at 200 °C for 60 min, and then the temperature was elevated from 50 °C to 550 °C under 5% H₂/Ar at a rate of 10 °C • min⁻¹. Pd²⁺/Pd⁰ ratios can be calculated by the Pd²⁺ loading through Pd²⁺ reduction peak integral with assistance of quantification function from facility and the total Pd loading from ICP test. Before the CO pulse test, 0.1 g sample was pretreated with 5% H₂/Ar at 300 °C for 3 min, and the CO pulse was conducted at 30 °C. X-ray photoelectron spectroscopy (XPS) was performed on a Thermo escalab 250Xi by using an Al Kα radiation source operating at 1486.6 eV. The binding energy and the Auger kinetic energy scales were referenced to the C 1 s signal at 284.6 eV from adventitious carbon. TGA was conducted on a NETZSCH thermogravimetric analyzer (STA 449 F5) equipped with a Mettler-Toledo balance, and the detailed inlet composition was shown in the results.

Diffuse reflectance infrared Fourier transform spectroscopy (DRIFTS) were conducted on a Bruker VERTEX 70 V equipped with an MCT detector and a high-temperature reaction chamber (Spectra-Tech collector) with ZnSe windows. The chamber was connected to a gas-distributing system. To eliminate the interference from water, the samples were initially pretreated with Ar in an infrared drying oven for 0.5 h to remove adsorbed water before each experiment. The DRIFTS spectra were collected in the range of 650–4000 cm⁻¹ with a resolution of 4 cm⁻¹. Prior to each test, the powder sample was pretreated with Ar at 200 °C for 0.5 h, and its absorbance spectra were collected at RT as the background. Before the hydrogenation reaction, NaNO₂ was impregnated on CTF-Pd according to a weight ratio of 6.89:80.

2.3. Activity test

The NO_x conversion into ammonia involves three steps, as shown in Scheme 1b: (a): NO_x adsorption. This work utilized a NaOH solution (pH=13~14) to adsorb and convert NO/NO₂ into nitrite under RT and atmospheric pressure. The NO/NO₂ ratio in the inlets was 1:1, and the flow rate was 20 mL/min. The adsorption process used 20 mL of NaOH solution as an adsorbent, and this process was maintained for 90 min to quantify the nitrate and nitrite concentrations by ion chromatography (IC) with conductivity detection (Thermo Fisher Scientific ICS-6000 system; ASRS Recycle mode; Ionpac AS11-HC column; 20 mM KOH as the eluent; 1 mL/min eluent flow rate). b): Direct nitrite hydrogenation into ammonia. Quantified the ammonia concentrations by ion chromatography (IC) with conductivity detection, (Thermo Fisher Scientific ICS-6000 system; CSRS Recycle mode; Ionpac CS12A column; 20 mM methanesulfonic acid as the eluent; 0.6 mL/min eluent flow rate) and an external standard (NH₄Cl as the external standard). Two milliliters of deionized water, 1 mmol of sodium nitrite (NaNO₂) and 80 mg of catalyst were added to a branched 15 mL glass tube. H₂ was supplied by a gasbag connected to the branch, and the whole suspension system was blended for 24 h under ambient conditions. The products were quantified by IC and external standard methods. In the cyclic activity test, the catalyst was filtered and washed with deionized water, and the dried catalyst was reused again without any pretreatment. (c): Ammonia desorption. To estimate ammonia release from the reaction system as a model test, the product solution was heated to 50 °C, and the temperature was maintained for 3 h. The residual ammonia concentration was quantified by IC.

2.4. Density functional theory (DFT) calculations

The geometry optimizations and frequency calculations were carried out using the B3LYP functional [38–40]. The van der Waals correction of Grimme's D3 scheme with Becke–Johnson damping (DFT-D3 (BJ)) was incorporated to describe the noncovalent interactions between the adsorbent and the adsorbate [41,42]. The 6–31 G (d,p) basis set was used for the nonmetal atoms (C, H, O and N), and the SDD effective core potential was used for the Pd atoms. For each geometric stationary point, the single-point energy calculations were performed using an extended 6–31 + +G(d,p) basis set for the nonmetal atoms the SMD solvation model to determine the effect of the solvent (water) [43]. H₃O⁺ was used as the proton donor in the calculations. The binding free energy (*G_b*) was calculated as follows: *G_b* = *G_{Pd-NO2}* - *G_{Pd}* - *G_{NO2}*, where *G_{Pd-NO2}* is the free energy of the complex consisting of the Pd catalyst model and nitrite, and *G_{Pd}* and *G_{NO2}* are the free energies of the Pd catalyst model and nitrite respectively. All the calculations were performed with the Gaussian 16 software package [44].

3. Results and discussion

3.1. DFT calculation of nitrite hydrogenation over Pd catalyst

Since N₂ is found to be the dominating nitrate/nitrite hydrogenation product previously, the simulation of nitrite hydrogenation is initially conducted to guide the catalyst design and preparation to improve the ammonia selectivity specifically. According to theoretical predictions of binding free energies (*G_b*), nitrite ions (NO₂⁻) adsorbs on single Pd²⁺ atoms (−1.13 eV) more easily than on Pd₁₃ (−0.80 eV) and single Pd⁰ atoms (−0.42 eV) (see Fig. 1b), illustrating the preferential capture sites of nitrite on the Pd²⁺ species during hydrogenation. To verify the results through B3LYP functional, TPSS and PBE0 functionals have been employed to optimize the geometry of Pd₁₃ cluster. The interactions between small molecules (H₂ and nitrite) and two Pd-based adsorbents (Pd₁₃ cluster and Pd²⁺ atom) were investigated subsequently, using TPSS and PBE0.

The calculated *G_b* also indicates nitrite adsorbs on single Pd²⁺ atoms more easily than on Pd₁₃, as shown in Table S1. Because B3LYP is suitable to calculate the hydrogenation processes of NO₂@Pd²⁺ model, only B3LYP is used in the subsequent calculations. Similar to the H₂ dissociation on the Pd(111) surface, the H–H bond of H₂ can be broken easily without an energy barrier when H₂ is located on the Pd₁₃ cluster. Therefore, hydrogen dissociation is likely dominant on the Pd nanoparticles in the presence of H₂. The migration of highly active H atoms from Pd₁₃ cluster to the substrate material could help trigger the hydrogenation reaction of *NO₂ on the Pd²⁺ sites. As shown in Fig. 1c, the hydrogenation process starts from the conversion of *NO₂ to *NO, in which the N–O bond is broken by one H atom and proton, yielding H₂O, and this reaction is an exothermic process (−0.55 eV). Since the isolated Pd²⁺ single-atom sites provides only one reactive site, the dissociation of N–O to *N and *O can be avoided, which may occur with the aid of adjacent active sites on the Pd surface. Consequently, the dissociation pathway is not included in the theoretical investigations. The most likely hydrogenation product of *NO in ammonia synthesis is *HNO. The free-energy changes revealed that this process is slightly endothermic (0.30 eV). Furthermore, the next hydrogenation of *HNO can be achieved through H attachment to the O atom, and the Δ*G* of this process (*HNO → *HNOH) is only 0.23 eV. The remaining hydrogenation reactions in ammonia formation, including the formation of two intermediate species (*H₂NOH and *NH₂), are exothermic processes. In N₂ synthesis, *NO hydrogenation to *NOH and the following conversion to *N are both endothermic processes (1.24 and 1.47 eV). In addition, the conversion of *N₂O to *N₂OH presents the highest energy increase of 1.32 eV. The DFT calculations reveal that N₂ formation is much more difficult than ammonia formation on the Pd²⁺ sites, therefore, the designed catalyst possessing Pd²⁺ single atoms and Pd nanoparticles is

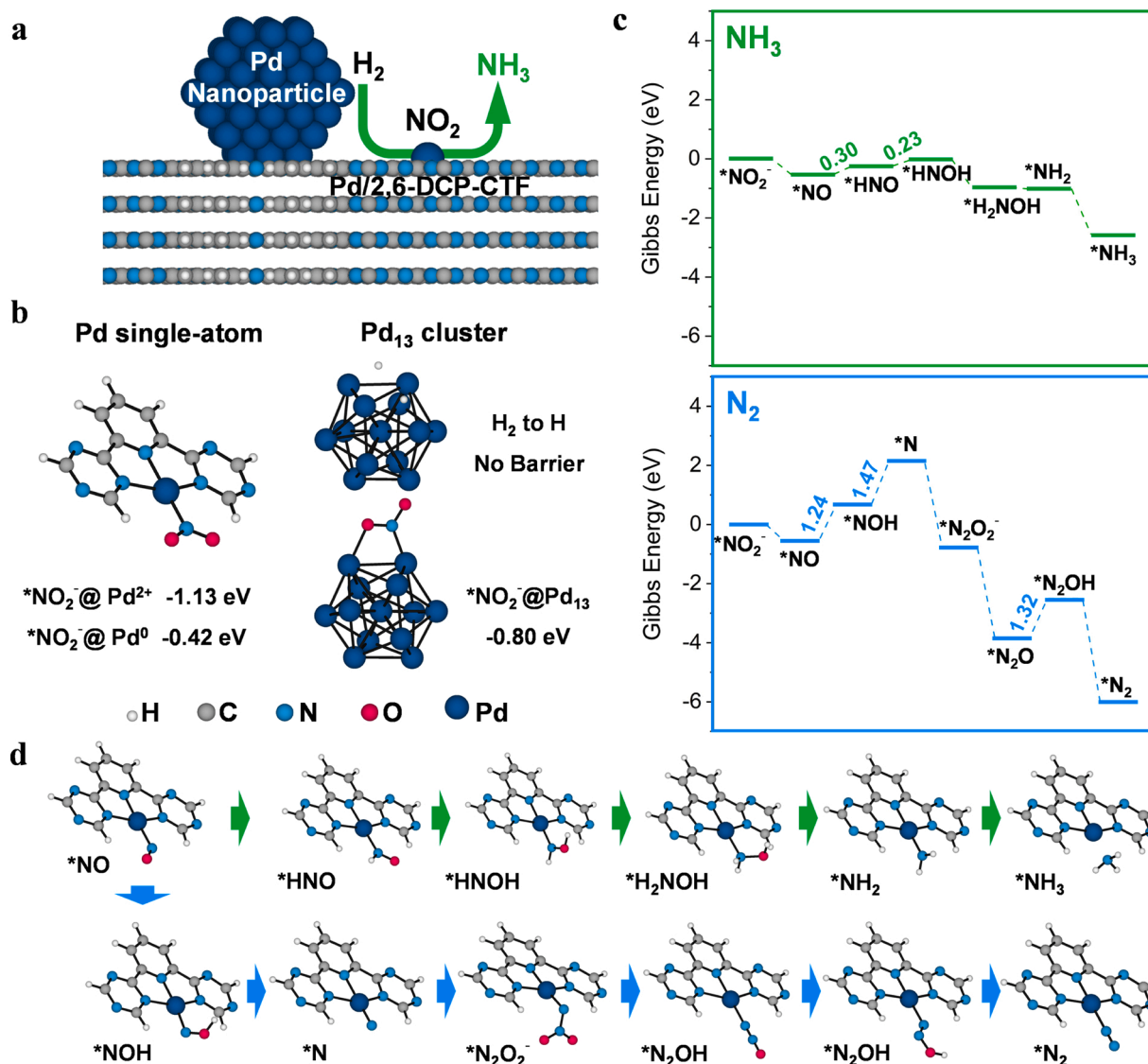


Fig. 1. Theoretical calculations of catalyst structure and reaction mechanism. (a) The designed catalyst model. (b) Optimized geometries of the calculation models of the Pd²⁺ single-atom catalyst ((2,6-di(1,3,5-triazin-2-yl)pyridine) palladium(2+/0)) and the Pd nanocatalyst (Pd₁₃ cluster). The values shown are the binding free energies between nitrite and the Pd²⁺/Pd⁰ single-atom model, and between nitrite and the Pd₁₃ cluster. (c) Free energy diagram of the minimum energy pathway for ammonia and N₂ as the main products. The values in green and blue represent the differences in the reaction free-energies in each pathway. Other possible reaction pathways for the final products of ammonia and N₂ are shown in Fig. S1. (d) Optimized geometries of the two minimum energy pathways.

likely to increase the ammonia selectivity. Moreover, the minor endothermic processes in the ammonia pathway imply that selective hydrogenation can occur under ambient conditions.

3.2. Characterization of Pd distribution and hydrogenation performance over Pd based catalysts

According to the above mechanism, the designed Pd^{2+/0}/CTF was synthesized, and Pd^{2+/0}/C₃N₄ [32] and Pd^{2+/0}/SiO₂ [33] were chosen as reference to estimate their nitrite conversion and ammonia selectivity. Table 1 displays the compositions and SSA results of Pd-based catalysts. CTF presented the highest SSA of 1349.968 m²/g, and the Pd loading decreased the SSA of all catalysts compared with the corresponding supports. In addition, the ICP results showed that the Pd contents were 4.9 wt% (Pd^{2+/0}/CTF), 4.6 wt% (Pd^{2+/0}/SiO₂) and 4.3 wt% (Pd^{2+/0}/C₃N₄). In addition, the available N and C contents are also summarized in Table 1 to analyze Pd surface enrichment later.

The N₂ adsorption-desorption isotherms in Fig. 2a and pore size distribution shown in Fig. 2b suggested the rich microporous structure

Table 1

The specific surface area (SSA) and compositions of all samples.

Sample	SSA (m ² /g)	Pd/N/C contents (wt %)	Sample	SSA (m ² /g)	Pd/N/C contents (wt %)
CTF	1349.9	0/7.09/46.37	Pd/CTF	1113.3	4.9/7.58/43.14
SiO ₂	177.6	/	Pd/SiO ₂	161.0	4.6/0/0
C ₃ N ₄	52.6	0/59.70/33.96	Pd/C ₃ N ₄	29.1	4.3/56.79/32.3

of CTF support, while SiO₂ and C₃N₄ exhibited meso-(macro)-porous structures, as shown in Fig. 2b. Moreover, the Pd loading decreased the amount of N₂ adsorption amount compared with corresponding pristine supports, but the pore distribution was not affected, implying that the Pd particles blocked partial pore structure. The XRD profiles in Fig. 2c are used to identify the material phases. The synthesized C₃N₄ exhibited typical peaks at 28°, 47° and 57° [37], and the peaks at 41° and 83° in

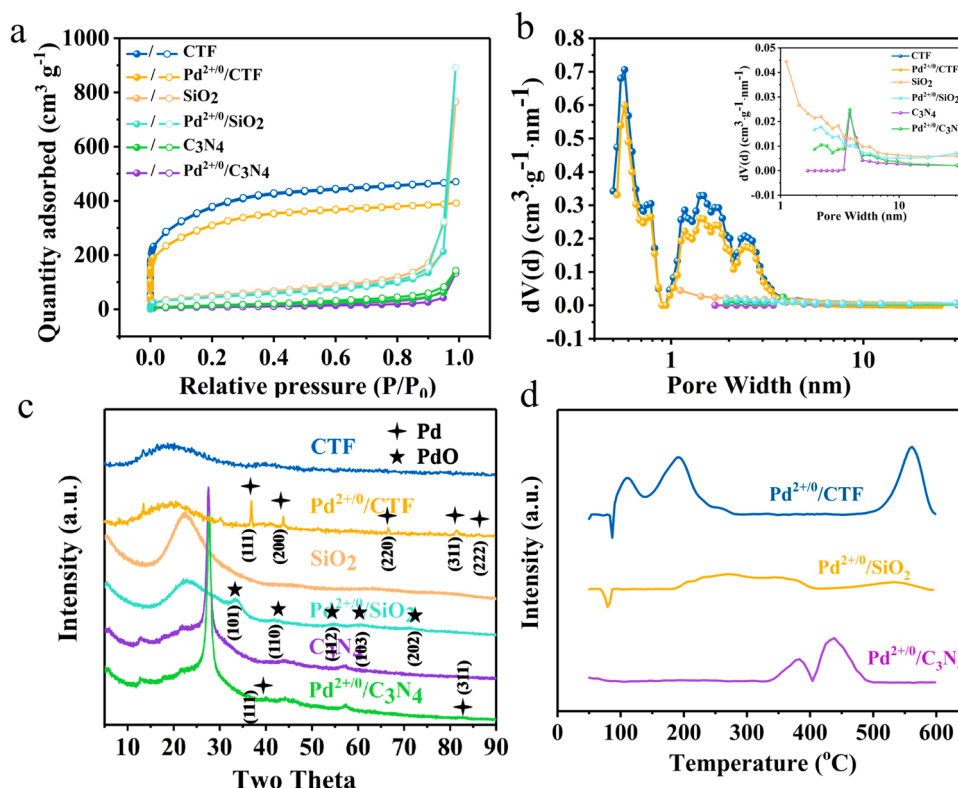


Fig. 2. (a) N₂ adsorption-desorption isotherms of CTF, Pd^{2+/0}/CTF, SiO₂, Pd^{2+/0}/SiO₂, C₃N₄ and Pd^{2+/0}/C₃N₄. (b) Pore distribution of CTF, Pd^{2+/0}/CTF, SiO₂, Pd^{2+/0}/SiO₂, C₃N₄ and Pd^{2+/0}/C₃N₄. (c) XRD profiles of CTF, Pd^{2+/0}/CTF, SiO₂, Pd^{2+/0}/SiO₂, C₃N₄ and Pd^{2+/0}/C₃N₄. (d) The H₂-TPR results of Pd^{2+/0}/CTF, Pd^{2+/0}/SiO₂ and Pd^{2+/0}/C₃N₄.

the XRD pattern of Pd^{2+/0}/C₃N₄ were ascribed to the Pd diffraction peaks. The commercial SiO₂ support presented typical broad peaks at 23.8° and 45°, and PdO diffraction peaks at approximately 34°, 42°, 55°, 61° and 71° were recorded. The Pd diffraction peaks of the Pd^{2+/0}/CTF sample at approximately 41°, 47°, 69°, 83° and 86° were also recorded. The various Pd species indicated from the XRD diffraction peaks suggested the support greatly affected the Pd distribution and locations.

Since the crystallinity of the synthesized CTF support was inferior, more methods were used to identify its framework structure. The XPS spectra in Fig. S2 presented three N 1s XPS peaks corresponding to pyridinic N (398.3 eV), pyrrolic N (401 eV) and graphitic N (403.9 eV). The C 1s XPS spectra in Fig. S3 showed three peaks at 284.5 eV, 286.5 eV and 288.4 eV, assigned to C-C, C-N and graphitized carbon, respectively [45]. These structures confirmed the formation of the triazine ring structure, and high-temperature calcination indeed caused the generation of a graphite phase, leading to partial skeleton collapse. The IR spectra in Fig. S4 presented the disappearance of the peaks corresponding to the monomers at approximately 3075 cm⁻¹ (C-H stretching vibration) and 2245 cm⁻¹ (ascribed to the -CN stretching vibration in the conjugated nitrile), illustrating the consumption of 2, 6-dicyanopyridine. In the spectra of the synthesized products, the appearance of peaks at 1180 cm⁻¹ and 1560 cm⁻¹ confirmed the formation of triazine ring structure, and Pd loading did not induce any new peaks, which only weakened the peak intensities at 1180 cm⁻¹ and 1560 cm⁻¹ [46].

Figs. 3a-3f showed the Pd distribution through TEM and HAADF-STEM images. Pd^{2+/0}/CTF and Pd^{2+/0}/SiO₂ presented uniform particle sizes below 5 nm (statistical results were shown in the inset), while Pd^{2+/0}/C₃N₄ possessed larger Pd nanoparticles between 2 and 25 nm. Massive light spots were detected in the HAADF-STEM images of Pd^{2+/0}/CTF and Pd^{2+/0}/C₃N₄, ascribed to atomically dispersed Pd species, but not in the images of the Pd^{2+/0}/SiO₂. The Pd dispersion estimated from

the CO pulse was 32.4%, 36.7% and 44.3% for Pd^{2+/0}/CTF, Pd^{2+/0}/SiO₂ and Pd^{2+/0}/C₃N₄, respectively. Although it seemed controversial for the Pd dispersion from the CO pulse result and TEM image for Pd^{2+/0}/C₃N₄, it was confirmed that electron irradiation easily induced the C₃N₄ support to melt and generated larger Pd slices, as shown in the TEM image. The weak Pd diffraction peaks in Fig. 2c also suggested that the Pd nanoparticle sizes were comparable to those of the other two samples. Therefore, the Pd distribution throughout Pd^{2+/0}/C₃N₄ was the highest, as the CO pulse result showed.

The H₂-TPR plots of the Pd^{2+/0}/CTF sample shown in Fig. 2d presented three Pd²⁺ reduction peaks at approximately 120 °C, 200 °C and 550 °C. Nevertheless, the Pd²⁺ reduction temperature over Pd^{2+/0}/C₃N₄ and Pd^{2+/0}/SiO₂ shifted to higher temperatures, especially for the Pd^{2+/0}/C₃N₄ sample, illustrating their inferior reducibility and the much stronger interaction between the Pd²⁺ and the supports. Likewise, the XPS spectra in Fig. S5-S7 revealed the coexistence of Pd²⁺ and Pd⁰ over the catalyst surface. The signals at binding energies of 337.9 eV and 343.2 eV were assigned to Pd²⁺ 3d_{5/2} and 3d_{3/2}, and those at 335.7 eV and 340.9 eV were ascribed to Pd⁰ 3d_{5/2} and 3d_{3/2} [52,53]. Peak fitting and area integration were performed, and the Pd²⁺/Pd⁰ ratios from H₂-TPR and XPS spectra are shown in Fig. 3i. The Pd^{2+/0}/CTF exhibited the highest Pd²⁺/Pd⁰ ratio, while Pd^{2+/0}/C₃N₄ exhibited the lowest ratio. To date, the impact of the support structure on the Pd distribution and valence states has been well analyzed.

Pd K-edge XANES were conducted to confirm the locations of Pd species and their charge. The experimental evidences are shown in Fig. 4 and Table S2. The white line intensity of Pd over Pd^{2+/0}/CTF in Pd K-edge XANES profiles is between Pd foil and PdO (Fig. 4a), and the adsorption edge in the inset also locates between Pd foil and PdO, demonstrating the Pd charge over Pd^{2+/0}/CTF is between 0~2 (but close to Pd²⁺). The FT k₃-weighted EXAFS spectra in R space of Pd^{2+/0}/CTF exhibit two obvious peaks (Fig. 4b). The first one at 1.94 Å represents the Pd-N coordination with coordination number of 3, proving the

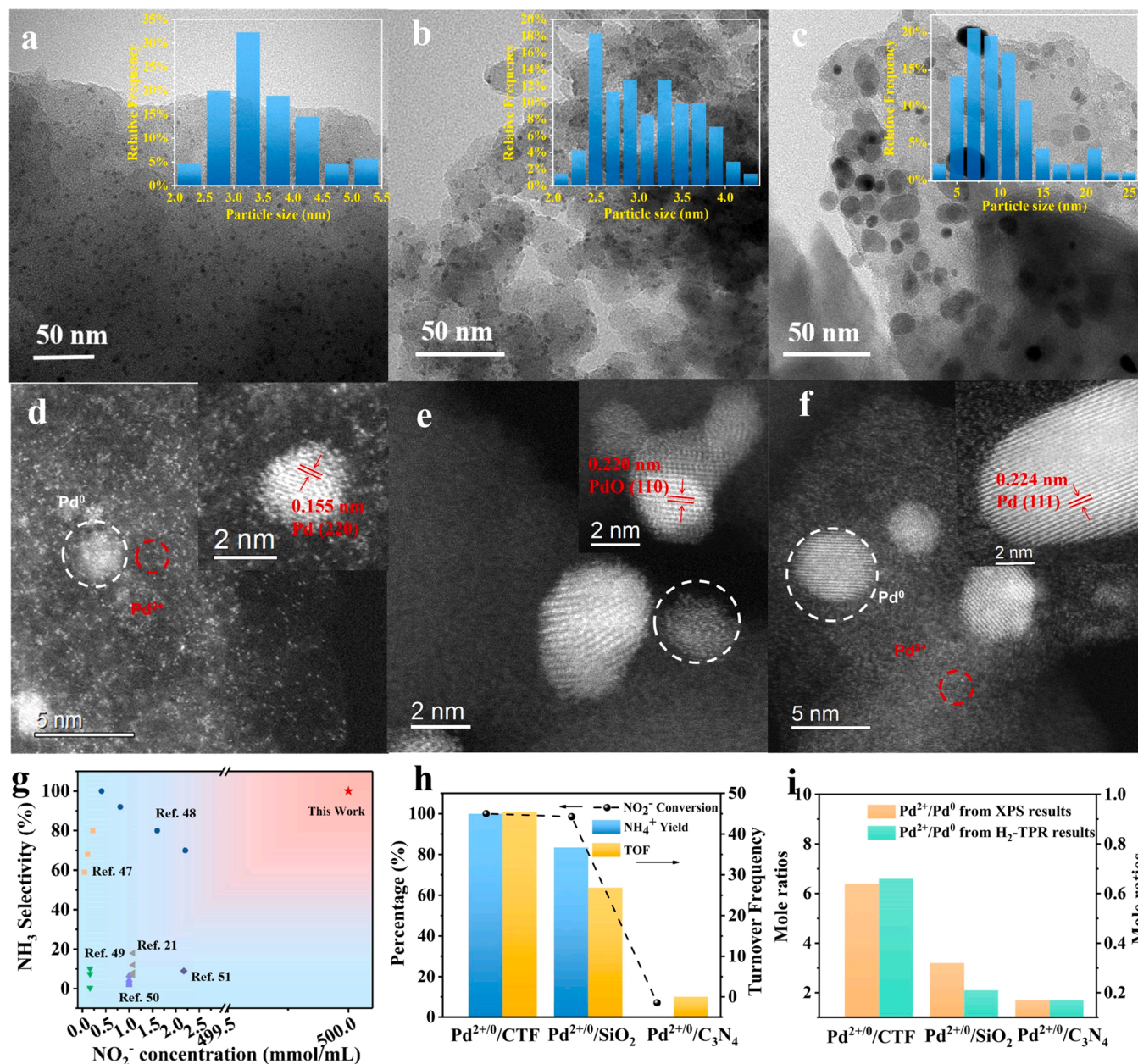


Fig. 3. Catalysts structure characterization and catalytic performance. TEM images of (a) Pd²⁺/CTF. (b) Pd²⁺/SiO₂ and (c) Pd²⁺/C₃N₄ and atomic-resolution HAADF-STEM images of (d) Pd²⁺/CTF. (e) Pd²⁺/SiO₂ and (f) Pd²⁺/C₃N₄. The scale bar in the TEM images represents 50 nm. (g) Ammonia selectivity as a function of nitrite concentration during hydrogenation. The data from the same reference were labeled by symbols of the same color [21, 47–51]. (h) The ammonia yield, nitrite conversion and the related TOF over three catalysts (TOF calculation is based on Pd loading from ICP and Pd dispersion from TEM results); (i) Pd²⁺/Pd⁰ ratios calculated from the XPS and H₂-TPR results.

existence of atomically dispersed Pd²⁺ sites. The other one at 2.92 Å is assigned to the Pd-Pd coordination with coordination number of 4, illustrating the formation of Pd particles on catalyst. And the triple-coordination between Pd and N benefited its catalytic reactivity during thermo-catalysis process.

In addition, the ammonia yield and TOF comparison under ambient conditions are shown in Fig. 3h, and the concentrations of nitrite and ammonia in solution were quantified by ion chromatography (IC). Pd²⁺/CTF catalyzed 100% of the nitrite into ammonia according to the detected N-containing products, but Pd²⁺/SiO₂ and Pd²⁺/C₃N₄ presented much lower ammonia yields of 83.4% and 0.2%, respectively. Fig. 3g shows a comparison between the activities of catalysts in this work and those reports in previous literatures. The comparison revealed that the ammonia yield over the designed Pd²⁺/CTF sample was

superior considering to the reactant concentration. Table S3 also listed the nitrite conversion as a function of pH value in solution, and Pd²⁺/CTF exhibited desired hydrogenation performance all the time. Consequently, the nitrite concentration was hundred times higher than previous literatures and the pH environment herein was versatile, directly affecting the energy utilization efficiency and operation costs during its scalability. Besides, even though the reaction conditions were completely different, the ammonia generation efficiency over Pd²⁺/CTF was still higher than recent ammonia generation report using photoelectrochemical NO_x conversion over TiO_x/CdS/CZTS catalyst under mild conditions [54].

To determine the reaction products other than ammonia that formed during the hydrogenation process over Pd²⁺/CTF, the effluent components of the reaction system were monitored by online mass

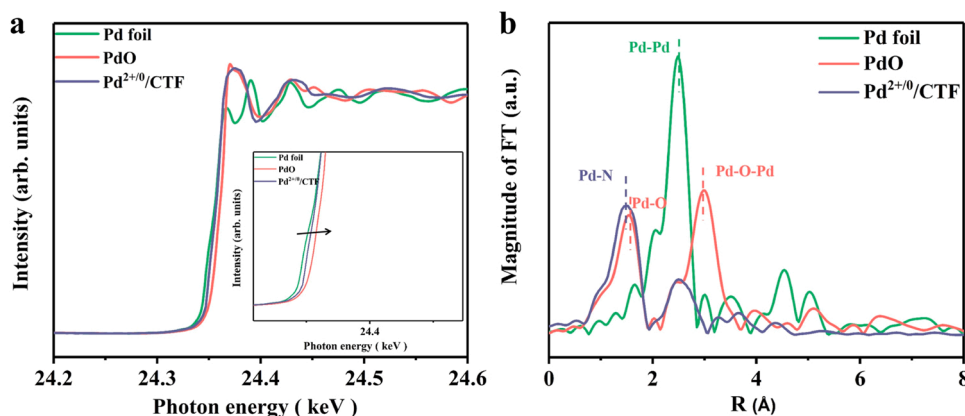


Fig. 4. (a) Pd K-edge XANES spectra for $\text{Pd}^{2+}/\text{CTF}$. Pd foil and PdO were used as the references. (b) Pd K-edge EXAFS in R space for $\text{Pd}^{2+}/\text{CTF}$. Pd foil and PdO were used as the references.

spectrometry (MS). Fig. S8 lists the H_2 , NH_3 and N_2 concentrations as a function of reaction time, and the system was purged with H_2 as the reactant. The dramatic initial fluctuation of H_2 and N_2 was induced by the valve switch. The results demonstrated that only the ammonia concentration rose until it stabilized with time on stream, illustrating the generation of ammonia and ammonia release during this process, while the N_2 concentration remained constant throughout the reaction. In addition, the scanning mode of the mass number showed signals of 2 (H_2 reactant), 4 (He carrier gas), 15 (NH), 17 (NH_3), and 18 (H_2O as solvent), but peaks corresponding to N_2 (28), NO (30), N_2O (44) and NO_2 (46) were not detected (Fig. S9 and 10). Besides, the isotope experiments with $^{15}\text{NO}_2$ as reactants for hydrogenation was also performed over $\text{Pd}^{2+}/\text{CTF}$, and the NMR spectra (Fig. S11) proved the N atoms all originated from $^{15}\text{NO}_2$ but not N from CTF framework.

As proposed in Fig. 1c, the Pd^0 and Pd^{2+} species were the major active sites for H_2 dissociation and nitrite hydrogenation, and the rate determining step was NO^* generation from nitrite dissociation during the ammonia synthesis. Since $\text{Pd}^{2+}/\text{CTF}$ presented the highest activity and the optimal $\text{Pd}^{2+}/\text{Pd}^0$ distribution among the three Pd-based samples, the effect of $\text{Pd}^{2+}/\text{Pd}^0$ ratios on ammonia selectivity over the $\text{Pd}^{2+}/\text{CTF}$ sample was estimated. The contrast experiments were performed on oxidized/reduced $\text{Pd}^{2+}/\text{CTF}$ to exaggerate the $\text{Pd}^{2+}/\text{Pd}^0$ ratio through O_2 (H_2) treatment at 300°C (350°C) for 40 min (6 h) prior to nitrite hydrogenation on the conditions of intact CTF structure (oxidized: $\text{Pd}^{2+}/\text{CTF}$, reduced: Pd^0/CTF). Compared with that of the pristine $\text{Pd}^{2+}/\text{CTF}$ sample, the Pd^{2+} reduction peaks in the H_2 -TPR plot disappeared below 400°C , as shown in Fig. S12, proving the partial reduction of Pd^{2+} to Pd^0 over Pd^0/CTF , while the Pd^{2+} reduction peaks became larger in the plot of $\text{Pd}^{2+}/\text{CTF}$. Similarly, the XPS results shown in Fig. S13-S14 also proved the increase of Pd^{2+} ratio on $\text{Pd}^{2+}/\text{CTF}$ and the decrease of Pd^{2+} ratio on Pd^0/CTF (see Table S4). Consequently, as shown in Fig. S15, nitrite hydrogenation tests exhibited 84% nitrite conversion and 54% ammonia selectivity over Pd^0/CTF and 79% nitrite conversion and 11% ammonia selectivity over $\text{Pd}^{2+}/\text{CTF}$. For the Pd^0/CTF sample, the decline in Pd^{2+} boosted the N_2 generation on Pd^0 sites in the presence of excess dissociated H atoms, while the shortage of Pd^0 over $\text{Pd}^{2+}/\text{CTF}$ greatly inhibited H atom production and induced a clear decrease in the ammonia yield over the Pd^{2+} sites, which proved that the Pd^0 species preferentially generated N_2 and the $\text{Pd}^{2+}/\text{Pd}^0$ ratio dominated the product dispersion. Similarly, the MS signal obtained in the mass scanning mode during this process provided evidence of N_2 generation, as shown in Fig. S16-S17. Since the CTF structure collapses quickly above 350°C , as shown in Fig. S18-S19, complete reduction of $\text{Pd}^{2+}/\text{CTF}$ was not performed above 350°C .

The DRIFTS of nitrite hydrogenation in the presence of 6% water over $\text{Pd}^{2+}/\text{CTF}$ were also showed in Figs. 5a-5c to demonstrate the influence of $\text{Pd}^{2+}/\text{Pd}^0$ ratio on the detected reaction intermediates.

During the nitrite hydrogenation process, a peak appeared at approximately 1032 cm^{-1} , which represented the nitrites on the $\text{Pd}^{2+}/\text{CTF}$ samples, and its decrease with the introduction of H_2 into the system illustrated its gradual consumption. The appearance of peaks at approximately 1023 cm^{-1} and 1054 cm^{-1} was ascribed to $-\text{NO}^*$ species and $-\text{NH}_3$ species [55,56], and the appearance of $-\text{NH}_3$ species always occurred after the $-\text{NO}^*$ species formed over three $\text{Pd}^{2+}/\text{CTF}$ samples, which was consistent with the ammonia generation rationale shown in Fig. 1c. New peaks appeared at 2830 and 2941 cm^{-1} and were assigned to the N-H

stretching mode of the generated ammonia ions [57]. In addition, only $\text{Pd}^{2+}/\text{CTF}$ presented stronger NH_3 peaks at 1054 cm^{-1} than the $\text{Pd}^{2+}/\text{CTF}$ (Pd^0/CTF) samples, since $\text{Pd}^{2+}/\text{CTF}$ showed an ammonia yield that was superior to the yields of the others. Thus far, due to the contrast between $\text{Pd}^{2+}/\text{Pd}^0$ ratios and ammonia yield in Figs. 3i and 3 h over three samples, it was concluded that the ammonia yield was not only determined by optimal coordination but also the desired $\text{Pd}^{2+}/\text{Pd}^0$ ratios during nitrite hydrogenation. Furthermore, the Pd/C ratio or Pd/N ratio identified by XPS and ICP, as shown in Table S5 indicated that Pd was enriched on the catalyst surface, since XPS mainly characterized elements on the sample surface. The surface enrichment of Pd species benefited the mass transfer of reactants during the heterogeneous reaction system, which could expel the impact of pore structure on the activity results among various catalysts. Generally speaking, the efficient cooperation between Pd^{2+} and Pd^0 during hydrogenation greatly relied on their location and reducibility on the supports. The structural investigations of CTF, SiO_2 and C_3N_4 revealed that the $\text{Pd}^{2+}/\text{CTF}$ possessed triazine groups and anchored Pd^{2+} and Pd^0 species around N atoms, exhibiting the highest reducibility. The layered structure of C_3N_4 sealed the Pd^{2+} and Pd^0 species tightly and presented inferior activity, and SiO_2 contained only Pd nanoparticles. The shortage of atomically dispersed Pd species led to moderate hydrogenation reactivity under ambient conditions.

3.3. The stability test of $\text{Pd}^{2+}/\text{CTF}$ and the bench test from NO_x into ammonia

Fig. 6 presents the catalytic stability of $\text{Pd}^{2+}/\text{CTF}$ through cyclic activity test. Throughout the 8 cycle evaluations, the ammonia selectivity was maintained at $\sim 100\%$, while the nitrite conversion maintained around 90% after 5 cycle's reaction. Fig. 6c presented.

the XRD profiles of the used $\text{Pd}^{2+}/\text{CTF}$ sample. Typical Pd (111) and (200) peaks were detected for all samples, and their peak intensities did not increase clearly. In Fig. 6d, the TEM images of fresh and used $\text{Pd}^{2+}/\text{CTF}$ samples showed an increased Pd particle size, which was partially responsible for the activity decrease in Fig. 6a. In addition, the ICP test of Pd revealed 5.0 wt% content on used $\text{Pd}^{2+}/\text{CTF}$ samples,

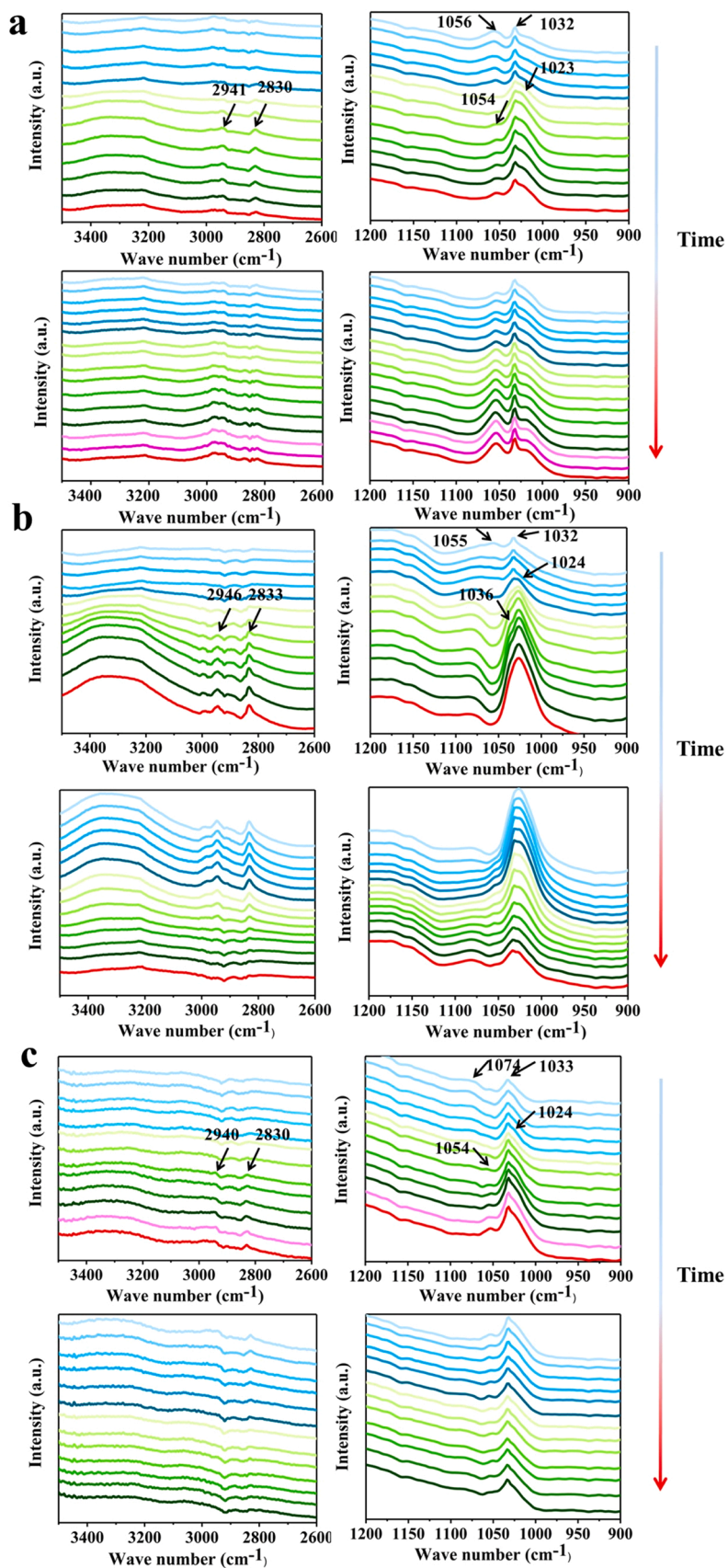


Fig. 5. DRIFTS spectra of nitrite hydrogenation over (a) $\text{Pd}^{2+/0}/\text{CTF}$, (b) $\text{Pd}^{2+}/\text{CTF}$ and (c) Pd^0/CTF under ambient conditions.

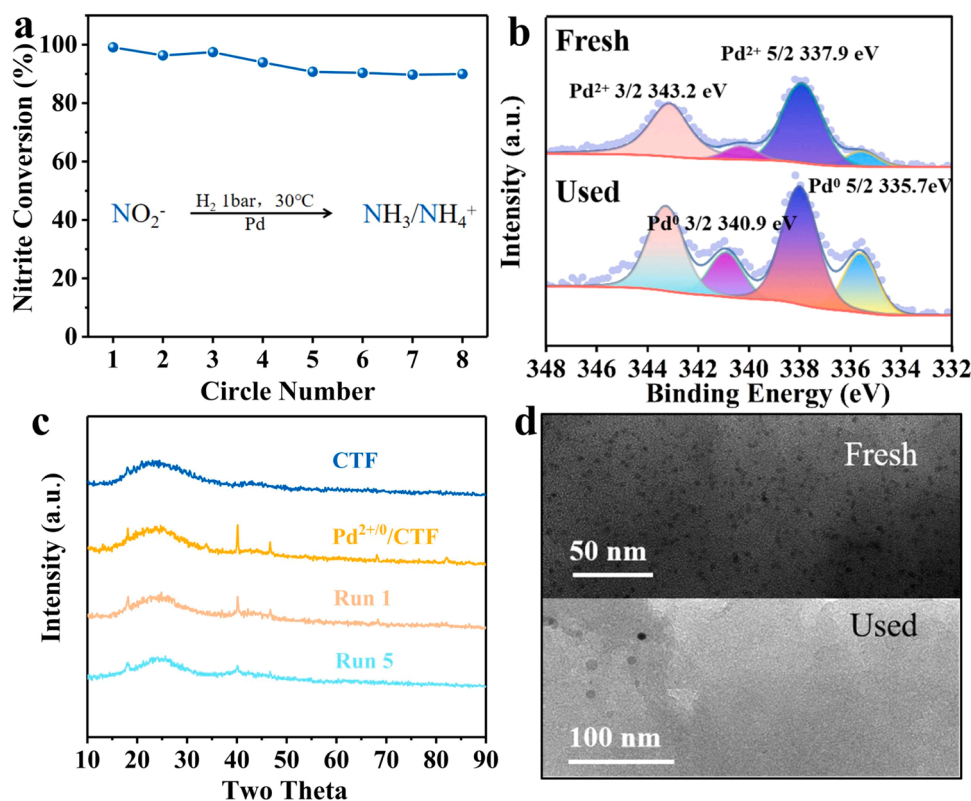


Fig. 6. The catalytic stability evaluation and corresponding bulk characterization of spent catalyst. (a) Cycle stability over $\text{Pd}^{2+/0}/\text{CTF}$; (b) the XPS spectra of Pd 3d over fresh and used $\text{Pd}^{2+/0}/\text{CTF}$; (c) XRD profiles of CTF, $\text{Pd}^{2+/0}/\text{CTF}$ and used $\text{Pd}^{2+/0}/\text{CTF}$ samples; (d) TEM images of fresh and used $\text{Pd}^{2+/0}/\text{CTF}$ after the hydrogenation reaction.

illustrating no Pd leaching during reaction process. As the XPS spectra of the fresh and used $\text{Pd}^{2+/0}/\text{CTF}$ in Fig. 6b, the used $\text{Pd}^{2+/0}/\text{CTF}$ after 8 cycles also revealed Pd^0 and Pd^{2+} signals, but the $\text{Pd}^{2+}/\text{Pd}^0$ ratio decreased from 6.4 to 2.3, demonstrating the gradual reduction of Pd^{2+} on the sample surface during the hydrogenation reaction, which led to Pd aggregation and was also responsible for the decreased activity shown in Fig. 6a. Finally, a model test was conducted to estimate the overall NOx conversion efficiency including single-pass NOx saturated adsorption in NaOH solution and subsequent $\text{Pd}^{2+/0}/\text{CTF}$ hydrogenation in 24 h. The results presented in Fig. S18 show that 70% NOx could be converted into nitrite under a gas flow rate of 20 mL/min, and the subsequent hydrogenation using $\text{Pd}^{2+/0}/\text{CTF}$ as a catalyst under ambient conditions could achieve 100% conversion of nitrite into ammonia. This model test clearly presented satisfactory ammonia synthesis efficiency, and the emitted NOx issue could be solved by continuous cycle adsorption.

4. Conclusion

In this work, we pioneer a new approach for NOx recycling through the hydrogenation of nitrite into ammonia, and the designed and screened out $\text{Pd}^{2+/0}/\text{CTF}$ catalyst exhibits a state-of-the-art ammonia yield. The DFT results initially pointed out the NO^* was a key intermediate and its hydrogenation into $^*\text{HNO}$ or $^*\text{NOH}$ would lead to generation of ammonia or N_2 in products, respectively. Meanwhile, the Pd^{2+} and Pd^0 species were necessary for nitrite hydrogenation and H_2 dissociation. The subsequent catalysts preparation successfully loaded Pd^{2+} and Pd^0 species through fabricating single atom Pd sites and Pd nanoparticles simultaneously on CTF support, and SiO_2 and C_3N_4 were also utilized to examine the influence of Pd-supports interaction on hydrogenation performance. The bulk characterization demonstrated Pd/CTF possessed the highest $\text{Pd}^{2+}/\text{Pd}^0$ ratios (6.4:1), and exhibited 100%

nitrite conversion with 100% ammonia selectivity under ambient condition. Through the comparison of Pd distribution and electronic properties among various catalysts, the easily reduced Pd^{2+} species on CTF support and the optimal $\text{Pd}^{2+}/\text{Pd}^0$ ratios enhanced the nitrite hydrogenation efficiency. The variation of $\text{Pd}^{2+}/\text{Pd}^0$ ratios on $\text{Pd}^{2+}/\text{CTF}$ (1:0) and Pd^0/CTF (0.57:1) decreased ammonia yield and illustrated excessive Pd^0 species benefited N_2 generation during nitrite hydrogenation. The DRIFTS of nitrite hydrogenation proved the generation of NO^* and only $\text{Pd}^{2+/0}/\text{CTF}$ revealed stronger NH_3 peaks at 1054 cm^{-1} than the $\text{Pd}^{2+}/\text{CTF}$ (Pd^0/CTF) for its superior performance on ammonia yield. The final model test revealed 70% NOx could be adsorbed by NaOH solution from single pass, and the $\text{Pd}^{2+/0}/\text{CTF}$ catalyst achieved 100% nitrite conversion into ammonia without byproducts. The subsequent ammonia desorption could be completely achieved at 50°C under heating condition and the NaOH solution is recycled as absorbent without pollutant emission. Moreover, the $\text{Pd}^{2+/0}/\text{CTF}$ catalyst still retained high catalytic activity when recycled 8 times. It presents satisfactory catalytic stability and gives a desired ammonia synthesis route from nitrite hydrogenation.

CRediT authorship contribution statement

W.D. conceived the concept and designed the research. J.Y. prepared the catalysts and carried out characterization measurements and activity tests. T.Y. carried out sample characterization, analyzed the results and wrote the first draft. L.S. conducted DFT calculations and wrote the corresponding section of the manuscript. X.F., S.Z., L.Z., G.R., R.T., D.Z. and Z.L. all discussed the results and help edit the manuscript.

Declaration of Competing Interest

The authors declare that they have no known competing financial

interests or personal relationships that could have appeared to influence the work reported in this paper.

Data availability

Data will be made available on request.

Acknowledgements

This work was supported by the National Key R&D Program of China (No. 2022YFA1503104, 2017YFA0204800), the National Natural Science Foundation of China (No. 21525315), the Fundamental Research Funds of Shandong University (No. 2019GN111), and the Shandong University Future Program for Young Scholars (No. 62460082064083). The authors thank Xiaojun Li and Haiyan Sui from Shandong University Core Facilities for Life and Environmental Sciences for their help with the TEM. Junxia Yang and Lei Sun contribute equally to this work.

Appendix A. Supporting information

Supplementary data associated with this article can be found in the online version at [doi:10.1016/j.apcatb.2023.122548](https://doi.org/10.1016/j.apcatb.2023.122548).

References

- J.D. Spengler, B.G. Ferris, D.W. Dockery, F.E. Speizer, Sulfur-dioxide and nitrogen-dioxide levels inside and outside homes and the implications on health-effects research, *Environ. Sci. Technol.* 13 (1979) 1276–1280.
- X.C. Meng, C. Li, S.P. Cui, L.L. Zhao, X.Z. Gong, Z.H. Wang, Scenario analysis of denitrification for chinese coal-fired power generation, *Mater. Sci. Forum* 814 (2015) 425–429.
- C.M.B. Lehmann, B.M. Kerschner, D.A. Gay, Impact of sulfur dioxide (SO₂) and nitrogen oxide (NO_x) emissions reductions on: acidic deposition in the united states, *EM Air Waste Manag. Assoc. Mag. Environ. Manag.* 65 (2015) 6–11.
- R. Li, Y. Zhu, Z. Zhang, C. Zhang, G. Fu, X. Yi, Q. Huang, F. Yang, W. Liang, A. Zheng, J. Jiang, Remarkable performance of selective catalytic reduction of NO_x by ammonia over copper-exchanged SSZ-52 catalysts, *Appl. Catal. B Environ.* 283 (2021), 119641.
- Z.F. Bai, B.B. Chen, Q. Zhao, C. Shi, M. Crocker, Positive effects of K⁺ in hybrid CoMn-K and Pd/Ba/Al₂O₃ catalysts for NO_x storage and reduction, *Appl. Catal. B Environ.* 249 (2019) 333–345.
- V. Rosca, M. Duca, M.T. de Groot, M.T.M. Koper, Nitrogen cycle electrocatalysis, *Chem. Rev.* 109 (2009) 2209–2244.
- J. Long, S. Chen, Y. Zhang, C. Guo, X. Fu, D. Deng, J. Xiao, Direct electrochemical ammonia synthesis from nitric oxide, *Angew. Chem. Int. Ed.* 59 (2020) 9711–9718.
- H. Niu, Z. Zhang, X. Wang, X. Wan, C. Kuai, Y. Guo, A feasible strategy for identifying single-atom catalysts toward electrochemical NO-to-NH₃ conversion, *Small* 17 (2021) 2102396.
- D. Kim, D. Shin, J. Heo, H. Lim, J.-A. Lim, H.M. Jeong, B.-S. Kim, I. Heo, I. Oh, B. Lee, M. Sharma, H. Lim, H. Kim, Y. Kwon, Unveiling electrode–electrolyte design-based NO reduction for NH₃ synthesis, *ACS Energy Lett.* 5 (2020) 3647–3656.
- P.-F. Sun, W.-L. Wang, X. Zhao, J.-S. Dang, Defective h-BN sheet embedded atomic metals as highly active and selective electrocatalysts for NH₃ fabrication via NO reduction, *Phys. Chem. Chem. Phys.* 22 (2020) 22627–22634.
- A. Hérissan, J.M. Meichtry, H. Remita, C. Colbeau-Justin, M.I. Litter, Reduction of nitrate by heterogeneous photocatalysis over pure and radiolytically modified TiO₂ samples in the presence of formic acid, *Catal. Today* 281 (2017) 101–108.
- D. Hao, Z.-g. Chen, M. Figliola, I. Stepniak, W. Wei, B.-J. Ni, Emerging alternative for artificial ammonia synthesis through catalytic nitrate reduction, *J. Mater. Sci. Technol.* 77 (2021) 163–168.
- A. Pintar, J. Batista, J. Levec, T. Kajituchi, Kinetics of the catalytic liquid-phase hydrogenation of aqueous nitrate solutions, *Appl. Catal. B Environ.* 11 (1996) 81–98.
- O.M. Ilinitch, L.V. Nosova, V.V. Gorodetskii, V.P. Ivanov, S.N. Trukhan, E. N. Gribov, S.V. Bogdanov, F.P. Cuperus, Catalytic reduction of nitrate and nitrite ions by hydrogen: investigation of the reaction mechanism over Pd and Pd–Cu catalysts, *J. Mol. Catal. A Chem.* 158 (2000) 237–249.
- T. Ren, K. Ren, M. Wang, M. Liu, Z. Wang, H. Wang, X. Li, L. Wang, Y. Xu, Concave-convex surface oxide layers over copper nanowires boost electrochemical nitrate-to-ammonia conversion, *Chem. Eng. J.* 426 (2021), 130759.
- L. Wei, D.-J. Liu, B.A. Rosales, J.W. Evans, J. Vela, Mild and selective hydrogenation of nitrate to ammonia in the absence of noble metals, *ACS Catal.* 10 (2020) 3618–3628.
- X. Zhao, X. Jia, Y. He, H. Zhang, X. Zhou, H. Zhang, S. Zhang, Y. Dong, X. Hu, A. V. Kuklin, G.V. Baryshnikov, H. Ågren, G. Hu, Two-dimensional BCN matrix inlaid with single-atom-Cu driven electrochemical nitrate reduction reaction to achieve sustainable industrial-grade production of ammonia, *Appl. Mater. Today* 25 (2021), 101206.
- Y. Han, X. Zhang, W. Cai, H. Zhao, Y. Zhang, Y. Sun, Z. Hu, S. Li, J. Lai, L. Wang, Facet-controlled palladium nanocrystalline for enhanced nitrate reduction towards ammonia, *J. Colloid Interface Sci.* 600 (2021) 620–628.
- Y.-J. Shih, Z.-L. Wu, Y.-H. Huang, C.-P. Huang, Electrochemical nitrate reduction as affected by the crystal morphology and facet of copper nanoparticles supported on nickel foam electrodes (Cu/Ni), *Chem. Eng. J.* 383 (2020), 123157.
- J. Li, J. Gao, T. Feng, H. Zhang, D. Liu, C. Zhang, S. Huang, C. Wang, F. Du, C. Li, C. Guo, Effect of supporting matrixes on performance of copper catalysts in electrochemical nitrate reduction to ammonia, *J. Power Sources* 511 (2021), 230463.
- H. Li, S. Guo, K. Shin, M.S. Wong, G. Henkelman, Design of a Pd–Au nitrite reduction catalyst by identifying and optimizing active ensembles, *ACS Catal.* 9 (2019) 7957–7966.
- K. Paredis, L.K. Ono, F. Beharfarid, Z. Zhang, J.C. Yang, A.I. Frenkel, B.R. Cuenya, Evolution of the structure and chemical state of Pd nanoparticles during the in situ catalytic reduction of NO with H₂, *J. Am. Chem. Soc.* 133 (2011) 13455–13464.
- J. Choi, H.-L. Du, C.K. Nguyen, B.H.R. Suryanto, A.N. Simonov, D.R. MacFarlane, Electroreduction of nitrates, nitrites, and gaseous nitrogen oxides: a potential source of ammonia in dinitrogen reduction studies, *ACS Energy Lett.* 5 (2020) 2095–2097.
- W. Dong, J. Hafner, H₂ dissociative adsorption on Pd(111), *Phys. Rev. B* 56 (1997) 15396–15403.
- L. Kuai, Z. Chen, S. Liu, E. Kan, N. Yu, Y. Ren, C. Fang, X. Li, Y. Li, B. Geng, Titania supported synergistic palladium single atoms and nanoparticles for room temperature ketone and aldehydes hydrogenation, *Nat. Commun.* 11 (2020) 48.
- X. Yang, Y. Wang, X. Wang, B. Mei, E. Luo, Y. Li, Q. Meng, Z. Jin, Z. Jiang, C. Liu, J. Ge, W. Xing, CO-tolerant PEMFC anodes enabled by synergistic catalysis between iridium single-atom sites and nanoparticles, *Angew. Chem. Int. Ed.* 60 (2021) 26177–26183.
- C. Rivera-Cárcamo, I.C. Gerber, I. del Rosal, B. Guichet, R. Castro Contreras, L. Vanoye, A. Favre-Régouillon, B.F. Machado, J. Audevard, C. de Bellefon, R. Philippe, P. Serp, Control of the single atom/nanoparticle ratio in Pd/C catalysts to optimize the cooperative hydrogenation of alkenes, *Catal. Sci. Technol.* 11 (2021) 984–999.
- A.V. Bavykina, A.I. Olivos-Suarez, D. Osadchii, R. Valecha, R. Franz, M. Makkee, F. Kapteijn, J. Gascon, Facile method for the preparation of covalent triazine framework coated monoliths as catalyst support: applications in C1 catalysis, *ACS Appl. Mater. Interfaces* 9 (2017) 26060–26065.
- M. Siebels, C. Schlüsener, J. Thomas, Y.-X. Xiao, X.-Y. Yang, C. Janiak, Rhodium nanoparticles supported on covalent triazine-based frameworks as re-usable catalyst for benzene hydrogenation and hydrogen evolution reaction, *J. Mater. Chem. A* 7 (2019) 11934–11943.
- M. Liu, L. Guo, S. Jin, B. Tan, Covalent triazine frameworks: synthesis and applications, *J. Mater. Chem. A* 7 (2019) 5153–5172.
- Y. Li, C. Lai, S. Liu, Y. Fu, L. Qin, M. Xu, D. Ma, X. Zhou, F. Xu, H. Liu, L. Li, Q. Sun, N. Wang, Metallic active-site engineering: a bridge between covalent triazine frameworks and high-performance catalysts, *J. Mater. Chem. A* 11 (2023) 2070–2091.
- Y. Wang, X. Wang, M. Antonietti, Polymeric graphitic carbon nitride as a heterogeneous organocatalyst: from photochemistry to multipurpose catalysis to sustainable chemistry, *Angew. Chem. Int. Ed.* 51 (2012) 68–89.
- X. Zeng, X. Hu, H. Song, G. Xia, Z.-Y. Shen, R. Yu, M. Moskovits, Microwave synthesis of zeolites and their related applications, *Microporous Mesoporous Mater.* 323 (2021), 111262.
- P. Kuhn, A. Thomas, M. Antonietti, Toward tailorable porous organic polymer networks: a high-temperature dynamic polymerization scheme based on aromatic nitriles, *Macromolecules* 42 (2009) 319–326.
- Y. Li, S. Zheng, X. Liu, P. Li, L. Sun, R. Yang, S. Wang, Z.-S. Wu, X. Bao, W.-Q. Deng, Conductive microporous covalent triazine-based framework for high-performance electrochemical capacitive energy storage, *Angew. Chem. Int. Ed.* 57 (2018) 7992–7996.
- G. Ren, J. Sun, S. Zhai, L. Yang, T. Yu, L. Sun, W. Deng, Ambient hydrogenation of carbon dioxide into liquid fuel by a heterogeneous synergistic dual single-atom catalyst, *Cell Rep. Phys. Sci.* 3 (2022), 100705.
- X. Wu, H. Ma, W. Zhong, J. Fan, H. Yu, Porous crystalline g-C₃N₄: bifunctional NaHCO₃ template-mediated synthesis and improved photocatalytic H₂-evolution rate, *Appl. Catal. B Environ.* 271 (2020), 118899.
- A.D. Becke, Density-functional exchange-energy approximation with correct asymptotic behavior, *Phys. Rev. A* 38 (1988) 3098–3100.
- A.D. Becke, Density-functional thermochemistry. III. The role of exact exchange, *J. Chem. Phys.* 98 (1993) 5648–5652.
- C. Lee, W. Yang, R.G. Parr, Development of the Colle-Salvetti correlation-energy formula into a functional of the electron density, *Phys. Rev. B* 37 (1988) 785–789.
- S. Grimme, J. Antony, S. Ehrlich, H. Krieg, A consistent and accurate ab initio parametrization of density functional dispersion correction (DFT-D) for the 94 elements H–Pu, *J. Chem. Phys.* 132 (2010), 154104.
- S. Grimme, S. Ehrlich, L. Goerigk, Effect of the damping function in dispersion corrected density functional theory, *J. Comput. Chem.* 32 (2011) 1456–1465.
- A.V. Marenich, C.J. Cramer, D.G. Truhlar, Universal solvation model based on solute electron density and on a continuum model of the solvent defined by the bulk dielectric constant and atomic surface tensions, *J. Phys. Chem. B* 113 (2009) 6378–6396.
- M.J. Frisch, G.W. Trucks, H.B. Schlegel, G.E. Scuseria, M.A. Robb, J.R. Cheeseman, G. Scalmani, V. Barone, G.A. Petersson, H. Nakatsuji, X. Li, M. Caricato, A.V.

- Marenich, J. Bloino, B.G. Janesko, R. Gomperts, B. Mennucci, H.P. Hratchian, J.V. Ortiz, A.F. Izmaylov, J.L. Sonnenberg, Williams, F. Ding, F. Lipparini, F. Egidi, J. Goings, B. Peng, A. Petrone, T. Henderson, D. Ranasinghe, V.G. Zakrzewski, J. Gao, N. Rega, G. Zheng, W. Liang, M. Hada, M. Ehara, K. Toyota, R. Fukuda, J. Hasegawa, M. Ishida, T. Nakajima, Y. Honda, O. Kitao, H. Nakai, T. Vreven, K. Throssell, J.A. Montgomery Jr., J.E. Peralta, F. Ogliaro, M.J. Bearpark, J.J. Heyd, E.N. Brothers, K.N. Kudin, V.N. Staroverov, T.A. Keith, R. Kobayashi, J. Normand, K. Raghavachari, A.P. Rendell, J.C. Burant, S.S. Iyengar, J. Tomasi, M. Cossi, J.M. Millam, M. Klene, C. Adamo, R. Cammi, J.W. Ochterski, R.L. Martin, K. Morokuma, O. Farkas, J.B. Foresman, D.J. Fox, Gaussian 16 Rev. C.01, Wallingford, CT, 2016.
- [45] X. Lan, Y. Li, C. Du, T. She, Q. Li, G. Bai, Porous carbon nitride frameworks derived from covalent triazine framework anchored Ag nanoparticles for catalytic CO₂ conversion, *Chem. Eur. J.* 25 (2019) 8560–8569.
- [46] L. Hao, N. Jing, B. Luo, B. Wang, Y. Zhang, Z. Tang, J. Yang, A. Thomas, L. Zhi, Structural evolution of 2D microporous covalent triazine-based framework toward the study of high-performance supercapacitors, *J. Am. Chem. Soc.* 137 (2015) 219–225.
- [47] R.S. Postma, R.B. Espinosa, L. Lefferts, Competitive adsorption of nitrite and hydrogen on palladium during nitrite hydrogenation, *Chemcatchem* 10 (2018) 3770–3776.
- [48] X. Huo, D.J. Van Hoomissen, J. Liu, S. Vyas, T.J. Strathmann, Hydrogenation of aqueous nitrate and nitrite with ruthenium catalysts, *Appl. Catal. B Environ.* 211 (2017) 188–198.
- [49] Z. Zhang, W. Shi, W. Wang, Y. Xu, X. Bao, R. Zhang, B. Zhang, Y. Guo, F. Cui, Interfacial electronic effects of palladium nanocatalysts on the by-product ammonia selectivity during nitrite catalytic reduction, *Environ. Sci. Nano* 5 (2018) 338–349.
- [50] Z. Zhang, J. Lu, B. Zhang, W. Shi, Y. Guo, F. Cui, Insight into the size effect of Pd nanoparticles on the catalytic reduction of nitrite in water over Pd/C catalysts, *Environ. Sci. Nano* 7 (2020) 2117–2129.
- [51] A. Devard, V.S. Aghemo, C.A. Caballero Dorantes, M. Gutierrez Arzaluz, F. Albana Marchesini, M. Alicia Ulla, Pd and In addition onto Au nanoparticles supported on TiO₂ as a catalytic formulation for NO₃ reduction in water, *React. Kinet. Mech. Catal.* 120 (2017) 39–54.
- [52] V. Muravev, G. Spezzati, Y.-Q. Su, A. Parastaev, F.-K. Chiang, A. Longo, C. Escudero, N. Kosinov, E.J.M. Hensen, Interface dynamics of Pd–CeO₂ single-atom catalysts during CO oxidation, *Nat. Catal.* 4 (2021) 469–478.
- [53] S.-Y. Ding, J. Gao, Q. Wang, Y. Zhang, W.-G. Song, C.-Y. Su, W. Wang, Construction of covalent organic framework for catalysis: Pd/COF-LZU1 in Suzuki–Miyaura coupling reaction, *J. Am. Chem. Soc.* 133 (2011) 19816–19822.
- [54] S. Zhou, K. Sun, C.Y. Toe, J. Yin, J. Huang, Y. Zeng, D. Zhang, W. Chen, O. F. Mohammed, X. Hao, R. Amal, Engineering kesterite based photocathode for photoelectrochemical ammonia synthesis from NO_x reduction (n/a), *Adv. Mater.* (2022) 2201670.
- [55] S.J. Huang, A.B. Walters, M.A. Vannice, Adsorption and decomposition of NO on lanthanum oxide, *J. Catal.* 192 (2000) 29–47.
- [56] J. Cai, C. Wang, Y. Liu, J. Ni, B. Lin, X. Wang, J. Lin, L. Jiang, Effect of pore-size distribution on Ru/ZSM-5 catalyst for enhanced N₂ activation to ammonia via dissociative mechanism, *J. Rare Earths* 38 (2020) 873–882.
- [57] X. Yang, B. Zhao, Y. Zhuo, Y. Gao, C. Chen, X. Xu, DRIFTS study of ammonia activation over CaO and sulfated CaO for NO reduction by NH₃, *Environ. Sci. Technol.* 45 (2011) 1147–1151.